Characteristic Basic Function Method accelerated by a new Physical Optics approximation for the scattering from a dielectric object

Christophe Bourlier

Progress In Electromagnetics Research B, Vol. 103, 177–194, 2023

Characteristic Basic Function Method Accelerated by a New Physical Optics Approximation for the Scattering from a Dielectric Object

Christophe Bourlier*

Abstract—This paper presents an efficient algorithm to calculate the primary basis functions (PBFs) of the characteristic basis function method (CBFM) for the scattering from a dielectric object. The use of the Poggio-Miller-Chang-Harrington-Wu (PMCHW) integral equation discretized by the Galerkin method of moments (MoM) with Rao-Wilton-Glisson basis functions leads to solving a linear system. For a collection of incident waves and for a given block, the CBFM needs to invert the whole PMCHW self-impedance matrix to calculate the PBFs. By decomposing the PMCHW impedance matrix into four sub-matrices of halved sizes, related to the electric and magnetic surface currents and their coupling, the computation of the PBFs is accelerated by using the impedance matrix derived from the electric field integral equation (EFIE) combined with the physical optics (named POZ) approximation. In addition, the PO developed by Jakobus and Landstorfer [35], named POJ and valid for a perfectly-conducting scatterer, is extended to a dielectric surface. Recently, the MECA (modified equivalent current approximation) Li and Mittra [29]) based on the tangent plane or Kirchhoff approximation has also been applied to expedite the PBF calculation. The presented method, HCBFM-POZ (H means halved), accelerated by the adaptive cross approximation (ACA), is tested and compared with CBFM-MECA and HCBFM-POJ on a cube and on a sphere. The numerical results show that HCBFM-POZ is valid for both the shapes, whereas the CBFM-MECA and HCBFM-POJ are not valid on a sphere.

1. INTRODUCTION

The method of moments (MoM) [1] has been widely used to analyze the electromagnetic scattering from dielectric objects. It converts the integral equation into a matrix equation with N unknowns (or degrees of freedom). Limited by the computational complexity and memory requirement, which scale with $\mathcal{O}(N^3)$ and $\mathcal{O}(N^2)$, respectively, the conventional MoM hardly handles the matrix equation with rapidly increasing unknowns. Many fast methods have been developed to alleviate this issue.

One kind of methods is to accelerate the MoM by combining iterative solvers with approximate compressed algorithms. For instance, based-conjugate gradient algorithms [2, 3], steepest descent fast multipole method [4–6], adaptive integral method [7–11], sparse-matrix canonical grid [12–16], and domain decomposition methods [17–20]. These techniques enable us to deal with electrically large objects. Nevertheless, the iterative solver is inefficient on solving the multiple excitations problems, because for each new excitation the iterative process needs to be resumed.

Another kind of methods is the direct solver based on the domain decomposition. It follows a similar strategy that utilizes the macro basis functions defined on the sub-domains to reduce the number of unknowns, such as the sub-domain multilevel approach [21], synthetic functions expansion [22], and characteristic basis function method (CBFM) [23]. The CBFM has been successfully applied to radiation and scattering problems.

Received 13 April 2023, Accepted 30 September 2023, Scheduled 22 November 2023
* Corresponding author: Christophe Bourlier (christophe.bourlier@univ-nantes.fr).
The author is with the IETR (Institut d'Electronique et des Technologies numéRiques) Laboratory, UMR CNRS 6164, Nantes Université, Polytech Nantes, La Chantrerie, Nantes, France.

For radiation problems, CBFM [20, 23–26] has been firstly developed to solve the electric field integral equation (EFIE) for the scattering analysis of objects that are perfect electric conductors (PECs) and more recently, in the case of dielectric bodies (for 2D and 3D problems) [27–33].

For a PEC, Bourlier [34] published a new physical optics approximation, named POZ, derived from the EFIE integral equation. The resulting impedance matrix $\bar{\mathbf{Z}}^{(\text{EFIE-POZ})}$ is then sparse (nearly $4N$ non-zeros values) since only self-facet interactions are accounted for. This allowed us to expedite the computation of the PBFs with a good accuracy. Another means to efficiently calculate the PBFs, without inverting the EFIE self-impedance sub-matrix of a block, is to apply the PO-surface current published by Jakobus and Landstorfer [35], named POJ. For different object shapes, comparing this method with the one based on $\bar{\mathbf{Z}}^{(\text{EFIE-POZ})}$, the simulations showed that CBFM-EFIE-POZ predicts very good results, and it is more accurate than CBFM-EFIE-POJ, which can be failed for some geometries, specially with curvature. The purpose of this paper is to extend these two formulations to a dielectric scatterer.

The use of the Poggio-Miller-Chang-Harrington-Wu (PMCHW) integral equation discretized by the Galerkin MoM with Rao-Wilton-Glisson (RWG) basis functions leads to solving a linear system $\bar{\mathbf{Z}}\mathbf{X} = \mathbf{b}$, where the PMCHW impedance matrix $\bar{\mathbf{Z}}$ is expressed as

$$\bar{\mathbf{Z}} = \begin{bmatrix} \bar{\mathbf{Z}}^{(\text{JJ})} & \bar{\mathbf{Z}}^{(\text{JM})} \\ -\bar{\mathbf{Z}}^{(\text{JM})} & \bar{\mathbf{Z}}^{(\text{MM})} \end{bmatrix}, \tag{1}$$

where $\bar{\mathbf{Z}}^{(\text{JJ})}$ and $\bar{\mathbf{Z}}^{(\text{MM})}$ are related to the electric and magnetic surface currents, respectively, and $\bar{\mathbf{Z}}^{(\text{JM})}$ to their coupling. In addition, from the EFIE impedance matrix $\bar{\mathbf{Z}}^{(\text{EFIE-}k_0)}$ of a PEC, $\bar{\mathbf{Z}}^{(\text{JJ})}$ and $\bar{\mathbf{Z}}^{(\text{MM})}$ are decomposed as

$$\begin{cases} \bar{\mathbf{Z}}^{(\text{JJ})} = \bar{\mathbf{Z}}^{(\text{EFIE-}k_1)} + \bar{\mathbf{Z}}^{(\text{EFIE-}k_2)} \\ \bar{\mathbf{Z}}^{(\text{MM})} = \dfrac{\bar{\mathbf{Z}}^{(\text{EFIE-}k_1)}}{\eta_1^2} + \dfrac{\bar{\mathbf{Z}}^{(\text{EFIE-}k_2)}}{\eta_2^2} \end{cases}, \tag{2}$$

where $\eta_i = \eta_0/\sqrt{\epsilon_{ri}}$, ϵ_{ri}, and $k_i = k_0\sqrt{\epsilon_{ri}}$ are the wave impedance, relative permittivity, and wavenumber of the medium i, respectively. Moreover, k_0 and $\eta_0 = 120\pi$ are the wavenumber and wave impedance in vacuum, respectively. $i = 1$ corresponds to the outer medium, in which the source illuminates the object, whereas $i = 2$, corresponds to the inner medium.

The purpose of this paper is to expedite the computation of the PBFs, related to $\bar{\mathbf{Z}}_{p,p}^{(\text{JJ})}$ and $\bar{\mathbf{Z}}_{p,p}^{(\text{MM})}$ of a block p, by applying the sparse impedance matrix $\bar{\mathbf{Z}}^{(\text{EFIE-POZ})}$ derived from EFIE-POZ. It is important to underline that $\bar{\mathbf{Z}}^{(\text{JM})}$ is considered as a coupling matrix, whereas the conventional CBFM computes the PBFs from the whole matrix (1). Due to the properties of $\bar{\mathbf{Z}}^{(\text{JJ})}$ and $\bar{\mathbf{Z}}^{(\text{MM})}$ (2), this new numerical scheme is easy to implement since $\bar{\mathbf{Z}}^{(\text{EFIE-}k_i)}$ is substituted for $\bar{\mathbf{Z}}^{(\text{EFIE-POZ-}k_i)}$. This also allows us to reduce, by a factor two, the size of the original matrix $\bar{\mathbf{Z}}$ (N becomes $N/2$) and to accelerate the PBF calculation as scaled $N_{\text{IW}}\mathcal{O}(2N^3)$ (LU plus SVD decompositions). N is the size of the matrix and N_{IW} the number of incident waves. To avoid inverting the PMCHW matrix for the computation of the PBFs, Chao Li and Mittra [29] applied the tangent plane or Kirchhoff approximation [36, 37], named MECA (modified equivalent current approximation). However, it is important to underline that the MECA can maintain a good accuracy only for objects with large radii of curvatures.

Following the generation of the CBFs, a new matrix with a much reduced size, namely the reduced matrix, is obtained. The resultant-reduced linear system enables the direct solution by using the LU decomposition algorithm. Moreover, the ACA algorithm [38–40] is incorporated for rapid calculation of the interaction matrices associated with the far-interaction blocks in the process of generating the reduced matrix. It is important to emphasize that the PO-based CBFs only serve as the macrobasis functions for an efficient representation of the final solution of the original problem. The mutual interaction between the sub-domains is taken into account rigorously when generating the combined reduced system.

The paper is organized as follows. Section 2 addresses a brief review of CBFM combined with three different PO formulations:

- POZ: Generalization of EFIE-PO [34] to the PMCHW, named POZ.

- POJ: Generalization of the Jakobus and Landstorfer [35] PO formulation, valid for a PEC surface, to a dielectric surface.
- MECA: Modified equivalent current approximation [29] valid for a dielectric surface.

Section 3 presents numerical results of the radar cross section (RCS) obtained from spheres and cubes. The last section gives concluding remarks.

The time convention $e^{-j\omega t}$ is used throughout this paper.

2. CBFM COMBINED WITH PO

2.1. PMCHW Integral Equation

From the PMCHW integral equations [28, 29, 37], the impedance matrix $\bar{\mathbf{Z}}$ is expressed from Eqs. (1) and (2), where an element is

$$\begin{cases} \bar{\mathbf{Z}}_{m,n}^{(\text{EFIE-}k_i)} = \langle \mathbf{f}_m, \boldsymbol{\mathcal{L}}_i(\mathbf{f}_n) \rangle \\ \bar{\mathbf{Z}}_{m,n}^{(\text{JM})} = \langle \mathbf{f}_m, \boldsymbol{\mathcal{K}}(\mathbf{f}_n) \rangle \end{cases}. \tag{3}$$

The vectors $\mathbf{f}_n$ and $\mathbf{f}_m$ are the basis and test (Galerkin method) RWG [41] functions, respectively, and the operator $\langle\ \rangle$ stands for the symmetric product between two vectorial functions defined as

$$\langle \mathbf{f}, \mathbf{g} \rangle = \int_S \mathbf{f}(\mathbf{r}) \cdot \mathbf{g}(\mathbf{r}) dS. \tag{4}$$

Moreover, the vectorial integro-differential operators $\boldsymbol{\mathcal{L}}_i$ and $\boldsymbol{\mathcal{K}}$, which depend on the position vector $\mathbf{r}$, are defined as

$$\begin{cases} \boldsymbol{\mathcal{L}}_i(\mathbf{X}) = -jk_i\eta_i \int_{S'} \left[\mathbf{X} + \dfrac{1}{k_i^2} \boldsymbol{\nabla} \left(\boldsymbol{\nabla}' \cdot \mathbf{X} \right) \right] G_i(\mathbf{r}, \mathbf{r}')\, dS' \\ \boldsymbol{\mathcal{K}}(\mathbf{X}) = \dfrac{}{\!\!\!\!\!\!\int\!\!\!\!\!\!\int}_{S'} \mathbf{X} \wedge \left[\boldsymbol{\nabla} G_1(\mathbf{r}, \mathbf{r}') + \boldsymbol{\nabla}' G_2(\mathbf{r}, \mathbf{r}') \right] dS' \end{cases}, \tag{5}$$

where the vectorial function $\mathbf{X}$ depends on $\mathbf{r}'$ (source point); $\boldsymbol{\nabla}$ denotes the nabla operator acting either on the position vector $\mathbf{r}$ or $\mathbf{r}'$ ($\boldsymbol{\nabla}'$); and G_i is the Green function defined as

$$G_i(\mathbf{r}, \mathbf{r}') = \frac{e^{-jk_i \|\mathbf{r} - \mathbf{r}'\|}}{4\pi \|\mathbf{r} - \mathbf{r}'\|}. \tag{6}$$

Symbol $\dfrac{}{\!\!\!\!\!\!\int\!\!\!\!\!\!\int}_{S'}$ is the Cauchy principal value defined for $\mathbf{r}' \neq \mathbf{r}$.

The elements $(b_m^{(\text{J})}, b_m^{(\text{M})})$ of the excitation vector $\mathbf{b} = [\mathbf{b}^{(\text{J})}; \mathbf{b}^{(\text{M})}]$ (MatLab notation) of the resulting linear system $\bar{\mathbf{Z}}\mathbf{X} = \mathbf{b}$ are expressed as

$$\begin{cases} b_m^{(\text{J})} = -\langle \mathbf{f}_m, \mathbf{E}_{\text{inc}} \rangle \\ b_m^{(\text{M})} = -\langle \mathbf{f}_m, \mathbf{H}_{\text{inc}} \rangle \end{cases}, \tag{7}$$

where $(\mathbf{E}_{\text{inc}}(\mathbf{r}), \mathbf{H}_{\text{inc}}(\mathbf{r}))$ are the electric and magnetic incident fields, respectively.

To solve the linear system $\bar{\mathbf{Z}}\mathbf{X} = \mathbf{b}$ efficiently, the impedance matrix $\bar{\mathbf{Z}}$ must be inverted. The conventional LU decomposition can be applied, but for an huge problem, this method is time consuming. The CBFM can be a good candidate to solve this issue. The CBFM parameters are listed in Table 1.

2.2. CBFM for a Dielectric Surface

The CBFM [20, 24, 28] begins by dividing the geometry of the object into P blocks. The impedance matrix $\bar{\mathbf{Z}}$ is then

$$\begin{bmatrix} \bar{\mathbf{Z}}_{1,1} & \bar{\mathbf{Z}}_{1,2} & \dots & \bar{\mathbf{Z}}_{1,P} \\ \bar{\mathbf{Z}}_{2,1} & \bar{\mathbf{Z}}_{2,2} & \dots & \bar{\mathbf{Z}}_{2,P} \\ \vdots & \vdots & \ddots & \vdots \\ \bar{\mathbf{Z}}_{P,1} & \bar{\mathbf{Z}}_{P,2} & \dots & \bar{\mathbf{Z}}_{P,P} \end{bmatrix} \begin{bmatrix} \mathbf{a}_1 \\ \mathbf{a}_2 \\ \vdots \\ \mathbf{a}_P \end{bmatrix} = \begin{bmatrix} \mathbf{b}_1 \\ \mathbf{b}_2 \\ \vdots \\ \mathbf{b}_P \end{bmatrix}, \tag{8}$$

Table 1. Definition of the notations introduced for CBFM and ACA. $\{P, n_{\mathrm{OL}}, \epsilon_{\mathrm{SVD}}, N_{\mathrm{IPW},p}\}$ are the inputs of CBFM. ϵ_{ACA} is the input of ACA. The remained values are numerically obtained from these inputs (outputs).

Name	Definition	Typical values
N_{Edge}	Total number of edges	Table 2
P	Number of blocks	Table 2
n_{OL}	Exceed edges due to the overlapping	1
ϵ_{SVD}	CBFM threshold of the SVD truncation	Table 2
$N_{\mathrm{IPW},p}$	CBFM plane wave number of block p	Eq. (10)
ϵ_{ACA}	ACA threshold	Table 2
$N_{\mathrm{IPW,SVD},p}$	Reduced value of $N_{\mathrm{IPW},p}$ after a SVD truncation	
$N_{\mathrm{Edge},p}$	Number of edges of a block p	
$N_{\mathrm{Edge,OL},p}$	Number of edges of a block with overlapping	
$\bar{N}_{\mathrm{Edge}} = \sum_{p=1}^{P} N_{\mathrm{Edge},p}$	Mean value of $N_{\mathrm{Edge},p}$ over $p \in [1;P]$	Table 2
$\bar{N}_{\mathrm{IPW}} = \sum_{p=1}^{P} N_{\mathrm{IPW},p}$	Mean value of $N_{\mathrm{IPW},p}$ over $p \in [1;P]$	Table 3
$\bar{N}_{\mathrm{IPW,SVD}} = \sum_{p=1}^{P} N_{\mathrm{IPW,SVD},p}$	Mean value of $N_{\mathrm{IPW,SVD},p}$ over $p \in [1;P]$	Table 3
ϵ_{RACA}	RACA threshold	$10\epsilon_{\mathrm{ACA}}$

where $\bar{\mathbf{Z}}_{p,p}$ is the self-impedance matrix of the block number p and $\bar{\mathbf{Z}}_{p_1,p_2}$ the coupling-impedance matrix between the blocks p_1 and p_2. In addition, the vectors $\mathbf{a}_p$ and $\mathbf{b}_p$ are the vectors $\mathbf{a}$ and $\mathbf{b}$ of the block number p, respectively.

Next, the primary basis functions (PBFs) are computed for a block p by solving the linear system [24, 28]

$$\bar{\mathbf{Z}}_{p',p'} \mathbf{Y}_{p',k_{\mathrm{IPW}}} = \mathbf{B}_{p',k_{\mathrm{IPW}}}. \tag{9}$$

It is important to underline that the symbol prime in the subscript of Eq. (9) indicates that the block is enlarged of some n_{OL} adjacent edges. This overlapping improves the accuracy of CBFM. The linear system (9) is solved from a collection of $2N_{\mathrm{IPW},p}$ bi-polarized incident plane waves $\{\mathbf{B}_{p',k_{\mathrm{IPW}}}\}$ ($k_{\mathrm{IPW}} \in [1; 2N_{\mathrm{IPW},p}]$), and the resulting vectors $\{\mathbf{Y}_{p',k_{\mathrm{IPW}}}\}$ are stored in a matrix $\bar{\mathbf{F}}_p$ of size $2N_{\mathrm{Edge},p} \times 2N_{\mathrm{IPW},p}$, where $N_{\mathrm{Edge},p}$ is the number of edges of a block p without overlapping. It means that the overlapped edges of $\mathbf{Y}_{p',k_{\mathrm{IPW}}}$ are removed.

The redundant information due to the overestimation of $N_{\mathrm{IPW},p}$ is eliminated via the use of a truncated singular value decomposition (SVD). It means that from a given threshold ϵ_{SVD}, the values, for which the moduli of the normalized eigenvalues are smaller than ϵ_{SVD}, are removed. The size of $\bar{\mathbf{F}}_p$ becomes $2N_{\mathrm{Edge},p} \times N_{\mathrm{IPW,SVD},p}$ with $N_{\mathrm{IPW,SVD},p} < 2N_{\mathrm{IPW},p}$.

It is important to underline that unlike a PEC scatterer, for a dielectric object [28], $N_{\mathrm{IPW},p}$ is the number of plane waves obtained for both the wavenumbers k_1 (outer medium) and k_2 (inner medium). The choice of $N_{\mathrm{IPW},p}$ must be relevant to avoid that the size of the matrix is too big because two decompositions, LU and SVD of complexities $\mathcal{O}(N^3_{\mathrm{Edge,OL},p})$, are required to calculate $\bar{\mathbf{F}}_p$. This point is crucial and addressed very little in the literature.

For a dielectric surface, extending the criterion proposed in [20, 42, 43] for a PEC, for a given wave number k_i, the number of plane waves N_{IPW} is defined as

$$N_{\mathrm{IPW}} = \min \left[\left\lfloor \frac{2\left(\mathrm{Re}(k_i) r_0 + 2\pi\right)^2}{n_{\mathrm{IPW}}}, N_{\mathrm{Edge,OL}} \right\rfloor \right] \tag{10}$$

where Re stands for the real part; symbol $\lfloor$ stands for the lower integer part; and r_0 is the sphere radius circumscribed to the block p. In addition, the number n_{IPW} is introduced because the simulations will show that N_{IPW} is either overestimated ($n_{\mathrm{IPW}} > 1$) or underestimated ($n_{\mathrm{IPW}} < 1$). Criterion (10) is related to the Nyquist sampling to ensure that there is no loss of information by decomposing any

source into a sum of plane waves. The "min" criterion on $N_{\text{Edge,OL}}$ is added because the size of $\bar{\mathbf{F}}_p$ does not have to exceed the original matrix size $\bar{\mathbf{Z}}_{p',p'}$ since the purpose is to reduce the number of freedom degrees.

For a PEC object, Huang and Sun [30] applied the adaptive cross approximation (ACA) [39, 40] to reduce, in advance, the number of incident plane waves N_{IPW}. For all the simulations presented in this paper, the number N_{IPW} calculated from (10) remains unchanged after ACA compression. It means that criterion (10) is a good choice.

The last stage of CBFM solves a reduced linear system $\bar{\mathbf{Z}}^{\text{R}}\mathbf{a}^{\text{R}} = \mathbf{b}^{\text{R}}$ defined as

$$\begin{bmatrix} \bar{\mathbf{Z}}^{\text{R}}_{1,1} & \bar{\mathbf{Z}}^{\text{R}}_{1,2} & \dots & \bar{\mathbf{Z}}^{\text{R}}_{1,P} \\ \bar{\mathbf{Z}}^{\text{R}}_{2,1} & \bar{\mathbf{Z}}^{\text{R}}_{2,2} & \dots & \bar{\mathbf{Z}}^{\text{R}}_{2,P} \\ \vdots & \vdots & \ddots & \vdots \\ \bar{\mathbf{Z}}^{\text{R}}_{P,1} & \bar{\mathbf{Z}}^{\text{R}}_{P,2} & \dots & \bar{\mathbf{Z}}^{\text{R}}_{P,P} \end{bmatrix} \begin{bmatrix} \mathbf{a}^{\text{R}}_1 \\ \mathbf{a}^{\text{R}}_2 \\ \vdots \\ \mathbf{a}^{\text{R}}_P \end{bmatrix} = \begin{bmatrix} \mathbf{b}^{\text{R}}_1 \\ \mathbf{b}^{\text{R}}_2 \\ \vdots \\ \mathbf{b}^{\text{R}}_P \end{bmatrix}, \tag{11}$$

where the submatrix $\bar{\mathbf{Z}}^{\text{R}}_{i,j}$ and subvector $\mathbf{b}^{\text{R}}_i$ are defined as

$$\begin{cases} \bar{\mathbf{Z}}^{\text{R}}_{i,j} = \bar{\mathbf{F}}^{\text{H}}_i \bar{\mathbf{Z}}_{i,j} \bar{\mathbf{F}}_j & [N_{\text{IPW,SVD},i} \times N_{\text{IPW,SVD},j}] \\ \mathbf{b}^{\text{R}}_j = \bar{\mathbf{F}}^{\text{H}}_j \mathbf{b}_j & [N_{\text{IPW,SVD},i} \times 1] \end{cases}. \tag{12}$$

Moreover, the symbol H stands for the conjugate transpose operator, and the indexes i and j go from 1 to P. The vector $\mathbf{a}_i$ of Eq. (8) is equal to $\mathbf{a}_i = \bar{\mathbf{J}}_i \mathbf{a}^{\text{R}}_i$.

The problem is then represented by the characteristic square matrix of size $(P\bar{N}_{\text{IPW,SVD}})^2$ instead of a square matrix of size $(2N_{\text{Edge}})^2 = (2P\bar{N}_{\text{Edge}})^2$, where $\bar{N}_{\text{IPW,SVD}} = (1/P)\sum_{p=1}^{P} N_{\text{IPW,SVD},p}$. If multiple excitations $\{\mathbf{b}\}$ (for instance, monostatic case) are calculated, then $\bar{\mathbf{Z}}^{\text{R}}$ (or the two matrices of the LU decomposition) and $\{\mathbf{J}_i\}$ (required to calculate $\mathbf{b}_i$) must be stored. The problem is then reduced by a factor $\beta^2 \approx (2\bar{N}_{\text{Edge}}/\bar{N}_{\text{IPW,SVD}})^2$ in comparison to a LU inversion of the whole matrix.

In Eq. (12), to accelerate the matrix-vector product, the coupling matrices $\{\bar{\mathbf{Z}}_{i,j}\}$ are compressed by using ACA. In addition, to further reduce the matrix rank, a second compression based on two QR decompositions, named RACA, is applied. This principle is summarized in [20], and two thresholds $\{\epsilon_{\text{ACA}}, \epsilon_{\text{RACA}}\}$ are then introduced. Typically $\epsilon_{\text{RACA}} = 10\epsilon_{\text{ACA}}$.

2.3. EFIE-CBFM Combined with POZ

From a conventional LU decomposition and for a given block p, Eq. (9) implies that the complexity to calculate the $2N_{\text{IPW}}$ PBFs is $2N_{\text{IPW}}\mathcal{O}(N^3_{\text{Edge,OL},p})$. In order to reduce this complexity, the PO approximation can be applied. Bourlier [26] derived the PO impedance matrix by injecting the PO current $\mathbf{J} = 2\hat{\mathbf{n}} \wedge \mathbf{H}_{\text{inc}}$ in EFIE. He showed that an element $Z^{(\text{EFIE-POZ})}_{m,n}$ of the resulting impedance matrix (in [26], its definition differs) is expressed as

$$\begin{aligned} -\frac{1}{\eta_1} Z^{(\text{EFIE-POZ})}_{m,n} &= \text{PV}\,(\text{MFIE}) \\ &= \frac{c_{m,n}}{12}\left(\sum_{i=1}^{3} \|\mathbf{V}_i\|^2 + \mathbf{V}_1 \cdot \mathbf{V}_2 + \mathbf{V}_1 \cdot \mathbf{V}_3 + \mathbf{V}_2 \cdot \mathbf{V}_3\right) + \frac{c_{m,n}}{2}\left[\mathbf{V}_m \cdot \mathbf{V}_n - \mathbf{V}_G \cdot (\mathbf{V}_m + \mathbf{V}_n)\right], \end{aligned} \tag{13}$$

where PV(MFIE) is the MFIE (magnetic field integral equation) principal value; $\{\mathbf{V}_i\}$ is the coordinates of the three vertices of the triangular facet of gravity center $\mathbf{V}_G$; $\{\mathbf{V}_{m,n}\}$ is the unshared vertices. Moreover, $c_{m,n} = s_m s_n L_m L_n/(4A)$, where $s_m = \pm 1$, $s_n = \pm 1$, $L_{m,n}$ is the edge length, and A is the facet area. Eq. (13) shows that the POZ impedance matrix is sparse since a facet interacts only with itself (no multiple reflections). This involves that only $4N_{\text{Edge},p}$ elements of the sub-impedance matrix are calculated (instead of $N^2_{\text{Edge},p}$). For different object shapes, comparing this method, named POZ, with the one based on Jakobus [35] (see Section 2.6), the simulations showed [26] that EFIE-CBFM-POZ predicts very good results, and it is more accurate than EFIE-CBFM-POJ, which can be failed for some geometries.

2.4. PMCHW-CBFM Combined with MECA: CBFM-MECA

To accelerate the PBF computation, Li and Mittra [29] developed a current-based PO method called the modified equivalent current approximation (MECA) and based on the tangent plane or Kirchhoff approximation [36, 37]. The electric and magnetic surface currents are

$$\left\{\begin{array}{l}\mathbf{J}=-\left(1-\boldsymbol{\mathcal{R}}_H\right)\cos\theta_1\left(\mathbf{H}_{\text{inc}}\cdot\hat{\mathbf{p}}_{\text{inc}}\right)\hat{\mathbf{q}}_{\text{inc}}+\left(1+\boldsymbol{\mathcal{R}}_V\right)\left(\mathbf{H}_{\text{inc}}\cdot\hat{\mathbf{q}}_{\text{inc}}\right)\left(\mathbf{n}\wedge\hat{\mathbf{q}}_{\text{inc}}\right)\\ \mathbf{M}=\left(1-\boldsymbol{\mathcal{R}}_V\right)\cos\theta_1\left(\mathbf{E}_{\text{inc}}\cdot\hat{\mathbf{p}}_{\text{inc}}\right)\hat{\mathbf{q}}_{\text{inc}}-\left(1+\boldsymbol{\mathcal{R}}_H\right)\left(\mathbf{E}_{\text{inc}}\cdot\hat{\mathbf{q}}_{\text{inc}}\right)\left(\mathbf{n}\wedge\hat{\mathbf{q}}_{\text{inc}}\right)\end{array}\right. , \tag{14}$$

where $\cos\theta_1=-\hat{\mathbf{k}}_{\text{inc}}\cdot\hat{\mathbf{n}}$, $\hat{\mathbf{q}}_{\text{inc}}=\hat{\mathbf{n}}\wedge\hat{\mathbf{k}}_{\text{inc}}/\left\|\hat{\mathbf{n}}\wedge\hat{\mathbf{k}}_{\text{inc}}\right\|$, $\hat{\mathbf{p}}_{\text{inc}}=\hat{\mathbf{q}}_{\text{inc}}\wedge\hat{\mathbf{k}}_{\text{inc}}$ and $\hat{\mathbf{k}}_{\text{inc}}$ is the incident wave direction. In addition, the Fresnel coefficients are defined as

$$\left\{\begin{array}{l}\boldsymbol{\mathcal{R}}_V(\theta_1)=\dfrac{\sqrt{\epsilon_{r2}}\cos\theta_1-\sqrt{\epsilon_{r1}}\cos\theta_2}{\sqrt{\epsilon_{r2}}\cos\theta_1+\sqrt{\epsilon_{r1}}\cos\theta_2}\\ \boldsymbol{\mathcal{R}}_H(\theta_1)=\dfrac{\sqrt{\epsilon_{r1}}\cos\theta_1-\sqrt{\epsilon_{r2}}\cos\theta_2}{\sqrt{\epsilon_{r1}}\cos\theta_1+\sqrt{\epsilon_{r2}}\cos\theta_2}\end{array}\right. , \tag{15}$$

where $\cos\theta_2=\sqrt{1-(\epsilon_{r1}/\epsilon_{r2})(1-\cos^2\theta_1)}$.

Like for a PEC, the solution of the linear system (9) for given extended block p and incident wave $\mathbf{B}$ is $\mathbf{Y}^{(\text{MECA})}=[\mathbf{Y}^{(\text{J-MECA})};\mathbf{Y}^{(\text{M-MECA})}]$, where their elements $(Y_n^{(\text{J-MECA})},Y_n^{(\text{M-MECA})})$ are expressed as

$$\left\{\begin{array}{l}Y_n^{(\text{J-MECA})}=\hat{\mathbf{t}}(\mathbf{r}_n)\cdot\mathbf{J}(\mathbf{r}_n)\\ Y_n^{(\text{M-MECA})}=\hat{\mathbf{t}}(\mathbf{r}_n)\cdot\mathbf{M}(\mathbf{r}_n)\end{array}\right. . \tag{16}$$

As shown in Fig. 1, $\hat{\mathbf{t}}$ is the mean normal vector to the nth edge in its middle $\mathbf{r}_n$, and $\hat{\mathbf{n}}$ is the mean normal vector to the adjacent triangles.

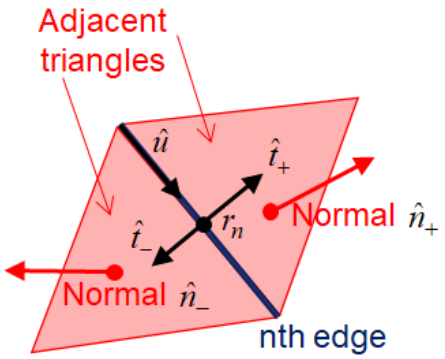

Figure 1. MECA and POJ approximations. $\hat{\mathbf{n}}_\pm$ is the normal to the adjacent triangles of the nth edge, $\hat{\mathbf{u}}$ its direction and $\hat{\mathbf{t}}_\pm$ its normals in the middle $\mathbf{r}_n$, on the left and right. $\hat{\mathbf{t}}_\pm=\hat{\mathbf{u}}\wedge\hat{\mathbf{n}}_\pm$, $\hat{\mathbf{t}}=(\hat{\mathbf{t}}_+-\hat{\mathbf{t}}_-)/2$ and $\hat{\mathbf{n}}=(\hat{\mathbf{n}}_++\hat{\mathbf{n}}_-)/2$.

2.5. PMCHW-CBFM Combined with EFIE-POZ: HCBFM-POZ

In order to extend the based-EFIE POZ impedance approach to a dielectric object, the properties of the sub-matrices $(\bar{\mathbf{Z}}^{(\text{JJ})},\bar{\mathbf{Z}}^{(\text{MM})})$ (2) depending on $\bar{\mathbf{Z}}^{(\text{EFIE-}k_i)}=-\eta_i\text{PV(MFIE)}$ (13) are used. This leads to

$$\left\{\begin{array}{l}\bar{\mathbf{Z}}^{\text{JJ-POZ}}=-\text{PV}\left(\text{MFIE}\right)\left(\eta_1+\eta_2\right)\\ \bar{\mathbf{Z}}^{\text{MM-POZ}}=-\text{PV}\left(\text{MFIE}\right)\left(\dfrac{1}{\eta_1}+\dfrac{1}{\eta_2}\right)\end{array}\right. , \tag{17}$$

where the MFIE principal value PV(MFIE) only depends on the geometry from Eq. (13).

In comparison to the CBFM-MECA, from HCBFM-POZ, the computation of the PBFs $(\bar{\mathbf{F}}_p^{(\text{JJ-POZ})}, \bar{\mathbf{F}}_p^{(\text{MM-POZ})})$ of size $N_{\text{Edge,OL},p} \times 2N_{\text{IPW}}$ is done twice on a halved size matrix. In Eq. (12), $\bar{\mathbf{F}}_p = [\bar{\mathbf{F}}_p^{(\text{JJ-POZ})}; \bar{\mathbf{F}}_p^{(\text{MM-POZ})}]$. Unlike MECA, with POZ an inversion is needed on a sparse matrix to calculate the PBFs.

It is important to underline that for the conventional CBFM, the PBFs are computed from the whole impedance matrix (1). For HCBFM (H means halved), the PBFs are computed from the sub-matrices $\{\bar{\mathbf{Z}}^{(\text{JJ})}, \bar{\mathbf{Z}}^{(\text{MM})}\}$ of halved size. It means that $\bar{\mathbf{Z}}^{(\text{JM})}$ is considered as a coupling sub-matrix for the reduced matrix calculation.

2.6. PMCHW-CBFM Combined with the Jakobus Formulation (POJ): HCBFM-POJ

Like in the previous paragraph, the Jakobus formulation, valid for a PEC surface, is extended to a dielectric surface by benefiting the structure of the PMCHW impedance matrix (2). This leads to

$$\begin{cases} \bar{\mathbf{Z}}^{(\text{JJ-POJ})} = \bar{\mathbf{Z}}^{(\text{EFIE-}k_1\text{-POJ})} + \bar{\mathbf{Z}}^{(\text{EFIE-}k_2\text{-POJ})} \\ \bar{\mathbf{Z}}^{(\text{MM-POJ})} = \dfrac{\bar{\mathbf{Z}}^{(\text{EFIE-}k_1\text{-POJ})}}{\eta_1^2} + \dfrac{\bar{\mathbf{Z}}^{(\text{EFIE-}k_2\text{-POJ})}}{\eta_2^2} \end{cases}, \tag{18}$$

where the subscript "POJ" refers to the Jakobus formulation. In addition, from Eq. (13), one has

$$Z_{n,n}^{(\text{EFIE-}k_i\text{-POJ})} = -\eta_i Z_{n,n}^{(\text{MFIE-}k_i\text{-POJ})}, \tag{19}$$

where $Z^{(\text{MFIE-}k_i\text{-POJ})}$ is an element of the MFIE PV impedance matrix. Since only the self-edge interactions are accounted for with POJ, this matrix is diagonal. From the MFIE, the resulting linear system writes $\bar{\mathbf{Z}}^{(\text{MFIE})}\mathbf{X}^{(\text{MFIE})} = \mathbf{b}^{(\text{MFIE})}$, where an element of $\mathbf{b}^{(\text{MFIE})}$ equals $b_m^{(\text{MFIE})} = -\langle \mathbf{f}_m, \hat{\mathbf{n}} \wedge \mathbf{H}_{\text{inc}} \rangle$ [2], and an element of $\mathbf{X}^{(\text{MFIE})}$ is $X_n^{(\text{MFIE})} = \hat{\mathbf{t}} \cdot \mathbf{J}(\mathbf{r}_n) = \hat{\mathbf{t}} \cdot [2\hat{\mathbf{n}} \wedge \mathbf{H}_{\text{inc}}(\mathbf{r}_n)]$. From Eq. (19) (Fig. 1), this yields

$$Z_{n,n}^{(\text{EFIE-}k_i\text{-POJ})} = \frac{\eta_i \langle \mathbf{f}_n, \hat{\mathbf{n}} \wedge \mathbf{H}_{\text{inc}} \rangle}{\hat{\mathbf{t}} \cdot [2\hat{\mathbf{n}} \wedge \mathbf{H}_{\text{inc}}(\mathbf{r}_n)]}. \tag{20}$$

The substitution of the above equation into Eq. (18) allows us to calculate $\bar{\mathbf{Z}}^{(\text{JJ-POJ})}$ and $\bar{\mathbf{Z}}^{(\text{MM-POJ})}$. Moreover, the left hand side of linear system (18) is expressed by Eq. (7). Thus, for given incident wave $\mathbf{B}$ and block p, a PBF takes the form $\mathbf{Y}^{\text{POJ}} = [\mathbf{Y}^{(\text{J-POJ})}; \mathbf{Y}^{(\text{M-POJ})}]$, where their elements $(Y_n^{(\text{J-POJ})}, Y_n^{(\text{M-POJ})})$ are expressed as

$$Y_n^{(\text{J-POJ})} = -\frac{\langle \mathbf{f}_n, \mathbf{E}_{\text{inc}} \rangle}{Z_{n,n}^{(\text{JJ-POJ})}} \quad \text{and} \quad Y_n^{(\text{M-POJ})} = -\frac{\langle \mathbf{f}_n, \mathbf{H}_{\text{inc}} \rangle}{Z_{n,n}^{(\text{MM-POJ})}}. \tag{21}$$

Like MECA approximation (16), no matrix inversion is required to compute the PBFs.

3. NUMERICAL RESULTS

The wavelength in free space λ_0 is 1 m, and the outer medium is vacuum ($\epsilon_{r1} = 1$). The azimuthal incident and scattering angles are $\phi_{\text{inc}} = \phi_{\text{sca}} = 0$. Table 2 lists the simulation parameters and CBFM inputs like the threshold ϵ_{SVD} and the number n_{IPW} introduced in Eq. (10).

3.1. Sphere of Radius $a = 1\lambda_0$ (Cases 1–3)

The sphere of radius $1\lambda_0$ is plotted in Fig. 2. For all simulations, the number of blocks $P = 8$, incidence angle $\theta_{\text{inc}} = 0$ ($-\hat{\mathbf{z}}$ direction), the polarization is VV, and the edge mean length $\bar{l}_{\text{Edge}}$ is $0.05\lambda_0$ to satisfy the condition $\bar{l}_{\text{Edge}} \leq \lambda_0/[10 \times \text{Re}(\sqrt{\epsilon_{r2}})]$, where ϵ_{r2} is the inner medium permittivity, and Re stands for the real part.

For $\epsilon_{r2} = 2$, Fig. 3 plots the RCS (radar cross section) in dBm^2 versus the scattering angle θ_{sca}. To better exhibit the difference, Fig. 4 plots the ratio $10|\log_{10}(\text{RCS}/\text{RCS}_{\text{REF}})|$ (dB) versus θ_{sca}, where RCS_{REF} is the reference RCS given by the Mie solution ([44], Section 6.1). In the legend, the labels mean:

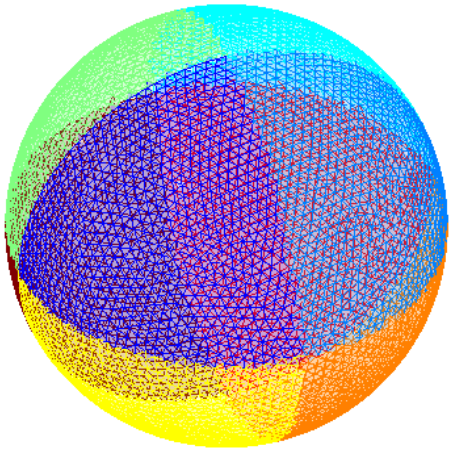

Figure 2. Sphere of radius equals $1\lambda_0$ ($N_{\text{Edge}} = 16,983$). A block is represented by a color and the edge mean length is $0.05\lambda_0$. The CBFM simulation parameters are listed in Table 2.

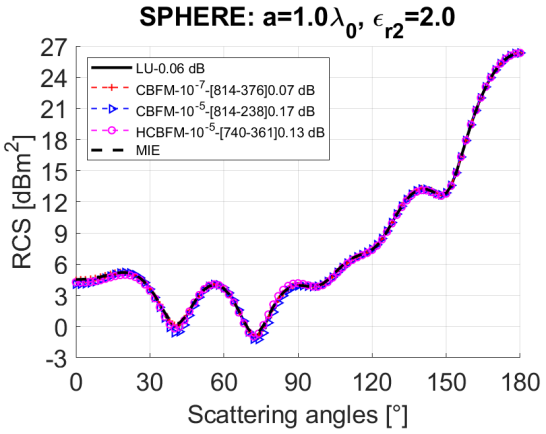

Figure 3. RCS in dBm^2 versus θ_{sca}. $a = 1\lambda_0$ (Fig. 2), $\theta_{\text{inc}} = 0$, VV polarization and $\epsilon_{r2} = 2$.

- LU: PMCHW linear system solved from a direct solver using the LU decomposition.
- CBFM: PMCHW linear system solved from the conventional CBFM [28, 29]. The PBFs are computed from the whole matrix (1).
- HCBFM: PMCHW linear system solved from the CBFM presented in this paper. The PBFs are computed from the two sub-matrices $(\bar{\mathbf{Z}}^{(\text{JJ})}, \bar{\mathbf{Z}}^{(\text{MM})})$ (2).
- MIE: Analytical solution of Mie.

In addition, one defines "CBFMi – ϵ_{SVD} – $[2\bar{N}_{\text{IPW}} - \bar{N}_{\text{IPW,SVD}}]$ – Dif", where the mean value Dif is defined as

$$\text{Dif} = \frac{1}{N_{\theta_{\text{sca}}}} \sum_{\theta_{\text{sca}}} 10 \left| \log_{10} \left(\frac{\text{RCS}}{\text{RCS}_{\text{REF}}} \right) \right|. \tag{22}$$

Table 3 (case 1) gives the values of $\bar{N}_{\text{IPW,SVD}}$ and Dif for CBFM and HCBFM combined with different formulations of PO. In comparison to the whole matrix of size $2N_{\text{Edge}} \times 2N_{\text{Edge}}$ ($N_{\text{Edge}} =$

Table 2. CBFM simulation parameters. $n_{\text{OL}} = 1$ for all cases. Cases 1–3: $N_{\text{Edge}} = 16,983$ and $P = 8$. Cases 4–6: $N_{\text{Edge}} = 16,983$ and $P = 8$. Case 7: $N_{\text{Edge}} = 24,321$ and $P = 24$. Case 8: $N_{\text{Edge}} = 41,472$ and $P = 26$. The number n_{IPW} is introduced in Eq. (10). The threshold ϵ_{SVD} is given for CBFM and HCBFM, respectively.

Case-Geometry	ϵ_{r2}	$\bar{N}_{\text{Edge}}$	$\bar{N}_{\text{Edge,OL}}$	n_{IPW}	ϵ_{SVD}
1-Sphere	2	2,123	2,330	1	$10^{-7}, 10^{-5}$
2-Sphere	2-0.2i	2,123	2,330	1	$10^{-7}, 10^{-5}$
3-Sphere	4	2,123	2,330	1	$10^{-7}, 10^{-5}$
4-Cube	2	1,764	1,980	0.5	$10^{-7}, 10^{-5}$
5-Cube	2-0.2i	1,764	1,980	0.5	$10^{-7}, 10^{-5}$
6-Cube	4	1,764	1,980	0.5	$10^{-7}, 10^{-5}$
7-Sphere	4-0.2i	1,013	1,216	1	-, 10^{-4}
8-Cube	4-0.2i	1,595	1,824	1	-, 10^{-6}

Table 3. CBFM is the conventional CBFM and HCBFM, that presented in this paper. Cases 1–3, the object is a sphere of radius $a = 1\lambda_0$. Cases 4–6, the object is a cube of length $L = 1.4\lambda_0$. Case 7, $a = 1.2\lambda_0$. Case 8, $L = 2.4\lambda_0$.

Case	CBFM	+MECA	HCBFM	+POJ	+POZ1
1: $2\bar{N}_{\text{IPW}}$	814	-	740	-	740
1: $\bar{N}_{\text{IPW,SVD}}$	376	-	361	-	349
1: Dif [dB]	0.07	-	0.13	-	0.06
2: $2\bar{N}_{\text{IPW}}$	814	-	740	-	740
2: $\bar{N}_{\text{IPW,SVD}}$	378	-	362	-	349
2: Dif [dB]	0.09	-	0.11	-	0.07
3: $2\bar{N}_{\text{IPW}}$	962	-	916	-	916
3: $\bar{N}_{\text{IPW,SVD}}$	473	-	480	-	466
3: Dif [dB]	0.15	-	0.18	-	0.05
4: $2\bar{N}_{\text{IPW}}$	1,314	1,314	1,252	1,252	1,252
4: $\bar{N}_{\text{IPW,SVD}}$	332	339	365	372	375
4: Dif [dB]	0.23	0.51	0.20	0.92	0.76
5: $2\bar{N}_{\text{IPW}}$	1,334	1,334	1,252	1,252	1252
5: $\bar{N}_{\text{IPW,SVD}}$	395	340	378	369	375
5: Dif [dB]	0.06	0.11	0.05	0.57	0.16
6: $2\bar{N}_{\text{IPW}}$	1,518	1,518	1,480	1,480	1,480
6: $\bar{N}_{\text{IPW,SVD}}$	466	409	497	501	499
6: Dif [dB]	0.19	2.02	0.16	2.66	0.63
7: $2\bar{N}_{\text{IPW}}$	-	-	923	-	923
7: $\bar{N}_{\text{IPW,SVD}}$	-	-	268	-	263
7: Dif [dB]	-	-	0.06	-	0.06
8: $2\bar{N}_{\text{IPW}}$	-	-	777	777	777
8: $\bar{N}_{\text{IPW,SVD}}$	-	-	398	368	394
8: Dif [dB]	-	-	0.11	064	0.24

$P\bar{N}_{\text{Edge}}$), the size of the CBFM characteristic matrix is $N_R \times N_R$, where $N_R = P\bar{N}_{\text{IPW,SVD}}$ and $\bar{N}_{\text{IPW,SVD}}$ is given in the legend of the figures as $[2\bar{N}_{\text{IPW}} - \bar{N}_{\text{IPW,SVD}}]$.

Figure 3 shows a good agreement with the Mie solution, especially for CBFM-$\epsilon_{\text{SVD}} = 10^{-7}$ and HCBFM-$\epsilon_{\text{SVD}} = 10^{-5}$, for which $\bar{N}_{\text{IPW,SVD}} = (376, 361)$ and the reduced factor $\beta = 2\bar{N}_{\text{Edge}}/\bar{N}_{\text{IPW,SVD}} = (5.65, 5.88)$, respectively. The CBFM needs a larger SVD threshold ϵ_{SVD} than HCBFM to obtain a similar number $\bar{N}_{\text{IPW,SVD}}$ of PBFs (or accuracy) because the size of the matrix is twice. Fig. 3 and Table 2 also show that the number $\bar{N}_{\text{IPW}}$, computed from Eq. (10), is smaller than $\bar{N}_{\text{Edge,OL}}$.

Figure 5 plots the ratio $10|\log_{10}(\text{RCS}/\text{RCS}_{\text{MIE}})|$ (dB) versus θ_{sca}, where the RCSs are computed from:

- HCBFM-POZ: PMCHW linear system solved from HCBFM, where the PBFs are computed from POZ (EFIE impedance matrix) (17).
- HCBFM-POZ1: Same as CBFM2-POZ, but the PBFs of the impedance matrix $\bar{\mathbf{Z}}^{(\text{MM})}$ are assumed to be equal to those of $\bar{\mathbf{Z}}^{(\text{JJ})}$.

As we can see, HCBFM-POZ based on the PO impedance matrix predicts better results than those calculated from HCBFM with a smaller number of PBFs (349 instead of 361). Moreover, the results of

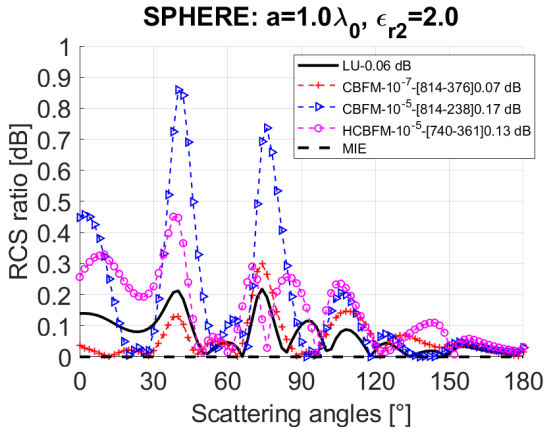

Figure 4. Ratio $10|\log_{10}(\mathrm{RCS}/\mathrm{RCS}_{\mathrm{MIE}})|$ [dB] versus θ_{sca}. The simulation parameters are the same as in Fig. 3.

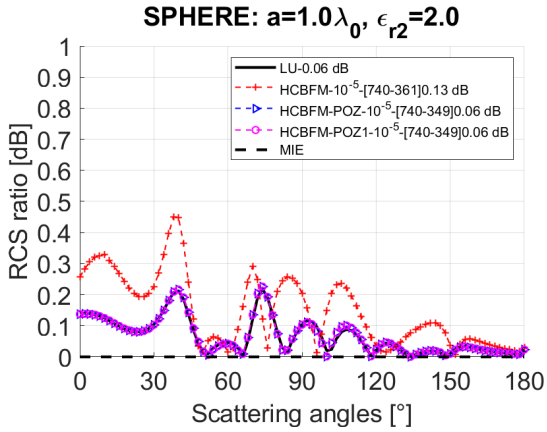

Figure 5. Ratio $10|\log_{10}(\mathrm{RCS}/\mathrm{RCS}_{\mathrm{MIE}})|$ versus θ_{sca}. The simulation parameters are the same as in Fig. 3.

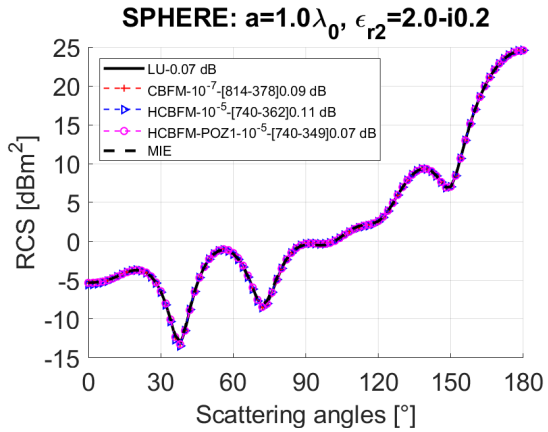

Figure 6. RCS in dBm^2 versus θ_{sca}. $a = 1\lambda_0$ (Fig. 2), $\theta_{\mathrm{inc}} = 0$, VV polarization and $\epsilon_{r2} = 2 - 0.2\mathrm{i}$.

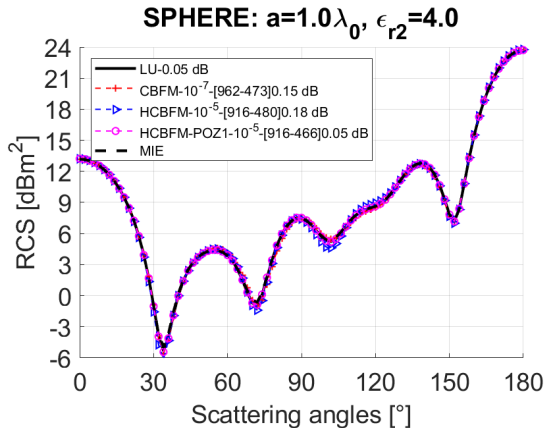

Figure 7. RCS in dBm^2 versus θ_{sca}. $a = 1\lambda_0$ (Fig. 2), $\theta_{\mathrm{inc}} = 0$, VV polarization and $\epsilon_{r2} = 4$.

HCBFM-POZ1 are the same as those obtained by HCBFM-POZ. From Eq. (17), one has

$$\frac{\bar{\mathbf{Z}}^{\text{MM-PO}}}{\bar{\mathbf{Z}}^{\text{JJ-PO}}} = \frac{\sqrt{\epsilon_{r1}\epsilon_{r2}}}{\eta_0^2}, \tag{23}$$

which explains that the PBFs calculated from $\bar{\mathbf{Z}}^{\text{JJ-PO}}$ and $\bar{\mathbf{Z}}^{\text{MM-PO}}$ are equal. In comparison to CBFM, this property expedites the computation because the impedance matrix size is divided by a factor two. It is important to underline that the results obtained from CBFM-MECA [29] and HCBFM-POJ, not depicted here, failed. This explains, in Table 3, why the symbol "-" (undefined) occurs.

Figures 6 and 7 plot the RCS in dBm^2 versus θ_{sca} for $\epsilon_{r2} = 2 - 0.2\mathrm{i}$ (case 2) and $\epsilon_{r2} = 4$ (case 3), respectively. Table 3 lists $(2N_{\mathrm{IPW}}, N_{\mathrm{IPW,SVD}}, \mathrm{Dif})$ versus the methods (CBFM, HCBFM, HCBFM-POZ1).

In comparison to $\epsilon_{r2} = 2$ (case 1), as $|\mathrm{Im}(\epsilon_{r2})|$ increases, $N_{\mathrm{IPW,SVD}}$ does not change significantly for a similar deviation from the Mie solution (Dif remains nearly constant). As $\mathrm{Re}(\epsilon_{r2})$ increases (from 2 to 4), more PBFs are required. This is a coherent result because as $\mathrm{Re}(\epsilon_{r2})$ grows, the wavelength decreases in the inner medium; therefore, a higher number of degrees of freedom is expected to model the surface currents.

In Table 3, for cases 1, 2 and 3, the number Dif shows that HCBFM-POZ1 is as accurate as HCBFM.

3.2. Cube of Length $L = 1.4\lambda_0$ (Cases 4–6)

The cube of length $L = 1.4\lambda_0$ is plotted in Fig. 8. For all simulations, the number of blocks $P = 8$, incidence angle $\theta_{\text{inc}} = 0$ ($-\hat{\mathbf{z}}$ direction), the polarization is VV, and the edge mean length $\bar{l}_{\text{Edge}}$ is $0.05\lambda_0$ to satisfy the condition $\bar{l}_{\text{Edge}} \leq \lambda_0/[10 \times \text{Re}(\sqrt{\epsilon_{r2}})]$, where ϵ_{r2} is the inner medium permittivity.

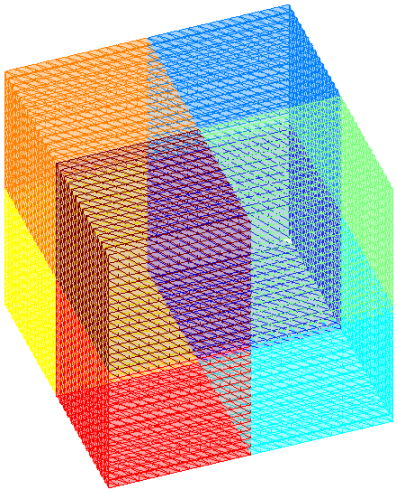

Figure 8. Cube of length $L = 1.4\lambda_0$ ($N_{\text{Edge}} = 14,112$). A block is represented by a color and the edge mean length is $0.06\lambda_0$. The CBFM simulation parameters are listed in Table 2.

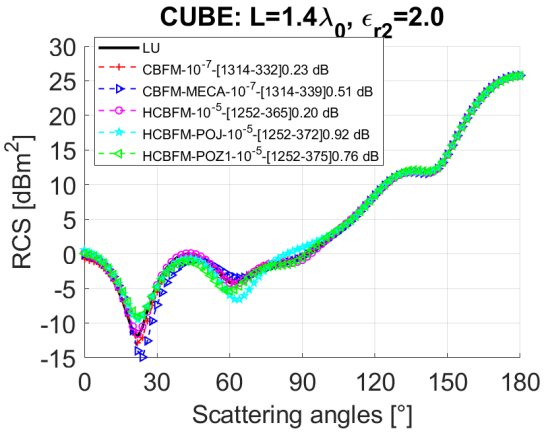

Figure 9. RCS in dBm^2 versus the scattering angle θ_{sca}. $L = 1.4\lambda_0$ (Fig. 8), $\theta_{\text{inc}} = 0$, VV polarization and $\epsilon_{r2} = 2$.

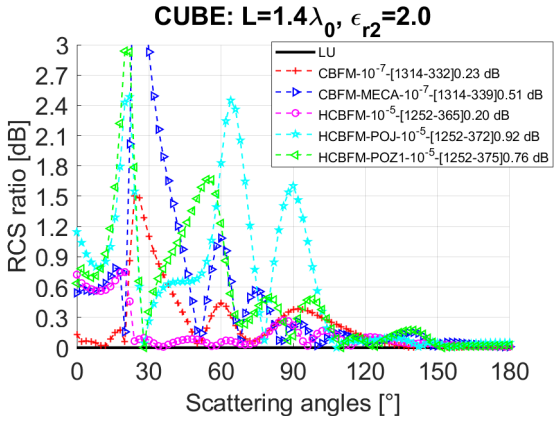

Figure 10. Ratio $10|\log_{10}(\text{RCS}/\text{RCS}_{\text{LU}})|$ [dB] versus the scattering angle θ_{sca}. The simulation parameters are the same as in Fig. 9.

For $\epsilon_{r2} = 2$, Fig. 9 plots the RCS in dBm^2 versus the scattering angle θ_{sca}. Fig. 10 plots the corresponding ratio $10|\log_{10}(\text{RCS}/\text{RCS}_{\text{LU}})|$ (dB) versus θ_{sca}. As we can see, the CBFM and HCBFM predict good results, except for low values of the RCS, and HCBFM is more accurate than CBFM because the number of PBFs is larger. Unlike the sphere, CBFM-MECA and HCBFM-POJ give satisfactory results, and their precisions are comparable. Moreover, HCBFM-POZ1 is less accurate

than HCBFM. In comparison to the sphere, the number of plane waves N_{IPW} is larger for a cube. In Table 2, $n_{\text{IPW}} = 0.5$ (from Eq. (10), N_{IPW} is twice) for the cube, whereas for the sphere $n_{\text{IPW}} = 1$.

For $\epsilon_{r2} = 2 - 0.2\text{i}$ and $\epsilon_{r2} = 4$, Figs. 11 and 12 plot the RCS in dBm^2 versus θ_{sca}. As $|\text{Im}(\epsilon_{r2})|$ increases, Fig. 11 reveals that CBFM and HCBFM predict better results as for $\text{Im}(\epsilon_{r2}) = 0$, and the number of PBFs $N_{\text{IPW,SVD}}$ slightly increases. When PO is applied, $N_{\text{IPW,SVD}}$ remains nearly the same as that obtained for $\text{Im}(\epsilon_{r2}) = 0$. In addition, the use of the different formulations of PO do not affect the accuracy. For HCBFM and for a threshold of $\epsilon_{\text{SVD}} = 10^{-6}$ (instead of $\epsilon_{\text{SVD}} = 10^{-5}$), results not depicted here show that the accuracy is better, but the number $N_{\text{IPW,SVD}}$ increases by 20%.

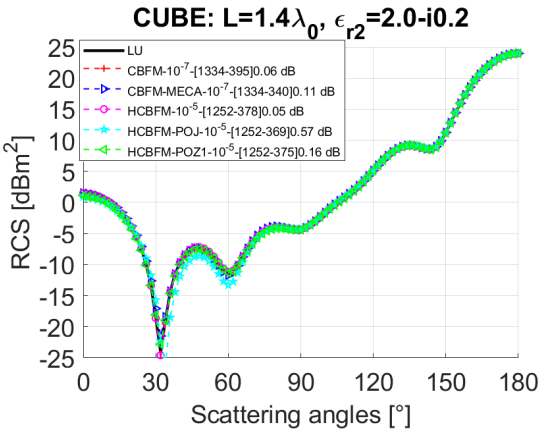

Figure 11. RCS in dBm^2 versus θ_{sca}. $L = 1.4\lambda_0$ (Fig. 8), $\theta_{\text{inc}} = 0$, VV polarization and $\epsilon_{r2} = 2 - 0.2\text{i}$.

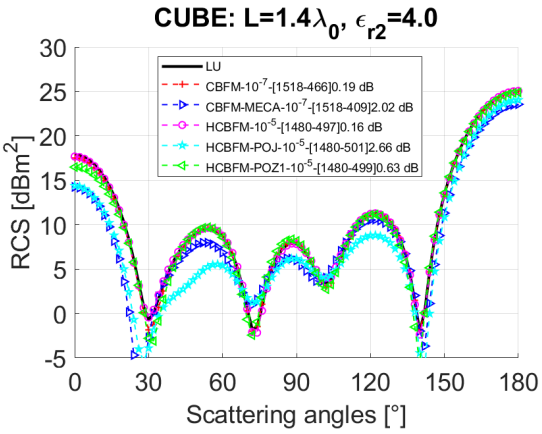

Figure 12. RCS in dBm^2 versus θ_{sca}. $L = 1.4\lambda_0$ (Fig. 8), $\theta_{\text{inc}} = 0$, VV polarization and $\epsilon_{r2} = 4$.

As $|\text{Re}(\epsilon_{r2})|$ increases, Fig. 12 reveals that the accuracies of CBFM and HCBFM do not change significantly in comparison to Fig. 9. Like for the sphere, the number $N_{\text{IPW,SVD}}$ grows in comparison to that obtained for $\epsilon_{r2} = 2$. In addition, Fig. 12 shows that HCBFM-POJ and CBFM-MECA deviate from LU, whereas HCBFM-POZ1 gives satisfactory results.

3.3. Hybridization with ACA (Cases 7–8)

In this section, HCBFM is combined with ACA.

Figure 13 plots the RCS in dBm^2 versus θ_{sca}. The sphere radius is $a = 1.2\lambda_0$ ($N_{\text{Edge}} = 24,321$); the number of blocks is $P = 24$; $\theta_{\text{inc}} = 0$; the polarization is VV; and $\epsilon_{r2} = 4 - 0.2\text{i}$. In the legend, within brackets, the numerical values are the two numbers $[\epsilon_{\text{ACA}}, \bar{\tau}_{\text{ACA}}]$ ($\epsilon_{\text{RACA}} = 10\epsilon_{\text{ACA}}$) defined in Table 1.

It is well known that the ACA compression is efficient for two distant blocks. Thus, ACA is not applied to connected blocks. For $P = 24$, the number of unconnected block pairs equals 398. For $\epsilon_{\text{ACA}} = 10^{-4}$, the number of compressed blocks pairs is 372, whereas for $\epsilon_{\text{ACA}} = 10^{-3}$, it is equal to 396. As expected, in Fig. 13, as ϵ_{ACA} increases, the ACA mean compression rate on the compressed block pairs increases and tends to 1. Typically, if $\tau_{\text{ACA}} \approx 1$, then a coupling matrix is approximated equal to the product of a column vector by a row vector. The mean rank of the compressed coupling matrices is then $\bar{r}_{\text{ACA}} \approx (1 - \bar{\tau}_{\text{ACA}})\bar{N}_{\text{Edge}}/2$.

For a matrix $\bar{\mathbf{Z}}$ of size $M \times N$, the ACA complexity scales $\mathcal{O}(r^2(N+M))$ due to the calculation of a norm between two matrices to stop the algorithm and determine the rank r. For a dielectric surface, the impedance matrix (1) is computed from three sub-matrices $(\bar{\mathbf{Z}}^{(\text{JJ})}, \bar{\mathbf{Z}}^{(\text{MM})}, \bar{\mathbf{Z}}^{(\text{JM})})$, which has to be compressed. To avoid calculating r for the three matrices, the rank r is only computed on $\bar{\mathbf{Z}}^{(\text{JJ})}$, and it is assumed to be the same for the two other matrices. This avoids calculating the norm and expedites the two next ACA compressions on $\bar{\mathbf{Z}}^{(\text{MM})}$ and $\bar{\mathbf{Z}}^{(\text{JM})}$. In addition, the two matrices $(\bar{\mathbf{U}}, \bar{\mathbf{V}})$ $(\bar{\mathbf{Z}} \approx \bar{\mathbf{U}}\bar{\mathbf{V}})$ are stored, which allows us to benefit the symmetrical properties of $(\bar{\mathbf{Z}}^{(\text{JJ})}, \bar{\mathbf{Z}}^{(\text{MM})}, \bar{\mathbf{Z}}^{(\text{JM})})$. Fig. 13 exhibits a very good agreement between the results with and without compression, which shows that ACA does not deteriorate the accuracy.

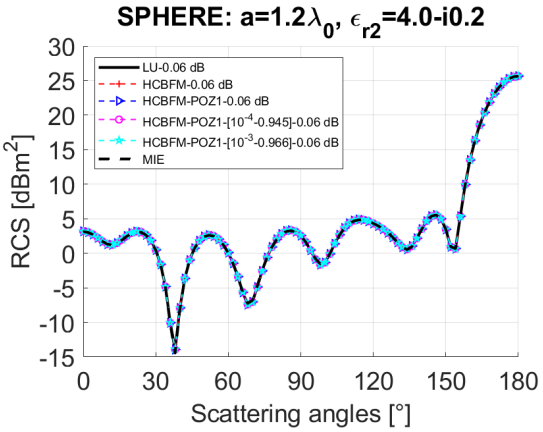

Figure 13. RCS in dBm^2 versus θ_{sca}. $a = 1.2\lambda_0$ ($N_{\mathrm{Edge}} = 24,321$ and $P = 24$), $\theta_{\mathrm{inc}} = 0$, VV polarization and $\epsilon_{r2} = 4 - 0.2\mathrm{i}$.

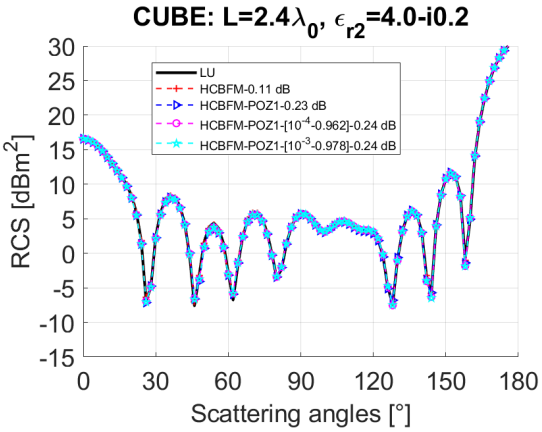

Figure 14. RCS in dBm^2 versus θ_{sca}. $L = 2.4\lambda_0$ ($N_{\mathrm{Edge}} = 41,472$ and $P = 26$), $\theta_{\mathrm{inc}} = 0$, VV polarization and $\epsilon_{r2} = 4 - 0.2\mathrm{i}$.

Figure 14 plots the RCS in dBm^2 versus θ_{sca}. The cube length is $L = 2.4\lambda_0$ ($N_{\mathrm{Edge}} = 41,472$); the number of blocks is $P = 26$, $\theta_{\mathrm{inc}} = 0$; the polarization is VV; and $\epsilon_{r2} = 4 - 0.2\mathrm{i}$. The number of unconnected block pairs equals 482 (on a total of $26^2 = 676$), and the number of compressed blocks is the same. As we can see, the results with compression match well with the HCBFM ones. The hybridization of POZ1 in HCBFM produces a slight difference from LU, which does not come from ACA.

3.4. Complexity and Comments on the Software MatLab

Figure 15 plots the computing time (in hours) in full and dashed lines versus the number of edges N_{Edge}. The filling time of the impedance matrix(es) is not included. The complexity is modelled as $C = aN_{\mathrm{Edge}}^n$, in which (a, n) are obtained from a linear regression, and their values are given in the legend. The last

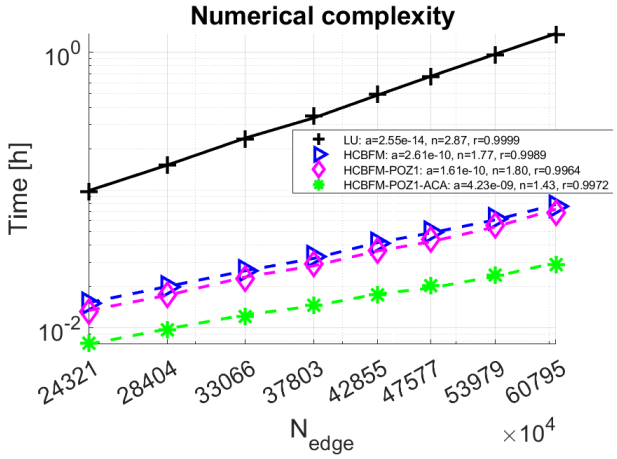

Figure 15. Computing time (in hours) versus the number of edges N_{Edge}, ranging from 24,321 to 60,795. The filling time of the impedance matrix(ces) is not included. The target is a sphere having a radius a ranging from $1.2\lambda_0$ to $1.9\lambda_0$ (mean edge length equals $0.05\lambda_0$) and its relative permittivity is $3 - 0.1j$. The number of blocks P ranges 21 to 45 and the edge mean number per block $\bar{N}_{\mathrm{Edge}}$ ranges from 1,158 to 1,578. The CBFM threshold is $\epsilon_{\mathrm{CBFM}} = 10^{-5}$ and the ACA threshold is $\epsilon_{\mathrm{ACA}} = 10^{-3}$.

number r is the regression coefficient (if $r = 1$ the regression is perfect). In Fig. 15, the symbols plots $C = aN_{\text{Edge}}^{n}$. As expected, the numerical complexity of LU is nearly $\mathcal{O}(N_{\text{Edge}}^{2.9})$ instead of $\mathcal{O}(N_{\text{Edge}}^{3})$ for the theoretical one. In Matlab, the function linsolve is applied to solve the linear system, and it is well optimized since it is parallelized. The use of HCBFM (without parallelization) allows us to reduce the complexity as $\mathcal{O}(N_{\text{Edge}}^{1.8})$, and its hybridization with POZ1 does not significantly change the complexity. Nevertheless, the computing time is slightly smaller than that obtained without hybridization. Indeed, as shown by Eq. (23), POZ1 assumes that the PBFs associated with the surface currents $\mathbf{J}$ and $\mathbf{M}$ are equal (POZ applied one time). The use of RACA allows us to further reduce the complexity since the block coupling impedance matrices are compressed, which accelerate the matrix-matrix products during the calculation of the reduced impedance matrix (stage 2, Eq. (12)). For a given geometry, $N_{\text{Edge}} = P\bar{N}_{\text{Edge}}$ is a constant. The complexity (value of n) can slightly change with respect to the value of P and $\bar{N}_{\text{Edge}}$. In Fig. 15, $\bar{N}_{\text{Edge}}$ ranges from 1,158 to 1,578. The block size should not exceed 2000–2500 unknowns in order that the calculation of the PBFs is fast. Its complexity is $\mathcal{O}(2\bar{N}_{\text{Edge}}^{3})$, corresponding to an LU inversion plus an SVD. Park et al. [45] published a paper on this issue.

For a perfect electric conductor, the theoretical complexity of CBFM and CBFM-POZ is derived in [34] (Figs. 14 and 15) and it is also compared with the numerical one, where a satisfactory agreement is obtained. Similar simulations, not depicted here, showed that the theoretical complexity overestimates the computing time.

To exploit the sparsity of the POZ impedance matrix, a basic iterative technique named "IT" is derived in [34]. For a dielectric surface, it is easy to generalize this algorithm. The theoretical complexity to compute the $2N_{\text{IPW}}$ PBFs of a single block is approximately $\mathcal{O}(4\bar{N}_{\text{Edge,OL}}KN_{\text{IPW}})$, whereas from LU, it is $\mathcal{O}(\bar{N}_{\text{Edge,OL}}^{3})$. Therefore, the time saving should be $\bar{N}_{\text{Edge,OL}}^{2}/(4KN_{\text{IPW}}) \gg 1$. With MatLab, numerical tests (1400 edges; sub-surface of size $(2\lambda)^2$) show that this ratio is of the order of 1. This shows that the function linsolve of MatLab, for which no loop is needed for the calculation of the PBFs, is well optimized (because parallelized) for multiple excitations. When CBFM is hybridized with POZ and an iterative solver (like IT or gradient conjugate), two loops are needed; the first one on the PBFs number and the second one, on the iteration k to obtain the convergence order K. This explains why the complexity (not shown here) is nearly the same between HCBFM-LU and HCBFM-POZ1-IT or HCBFM-POZ1-CG.

3.5. Memory Requirement

The memory requirement of HCBFM is:

$$M_{\text{HCBFM}} = \underbrace{2P\bar{N}_{\text{Edge}}^{2}}_{\{\bar{\mathbf{Z}}_{i,i}\}} + \underbrace{cP\bar{N}_{\text{Edge}}\bar{N}_{\text{IPW,SVD}}}_{\text{PBFs}} + \underbrace{\left(P\bar{N}_{\text{IPW,SVD}}\right)^{2}}_{\bar{\mathbf{Z}}_{R}}. \tag{24}$$

The first RHS term corresponds to the storage of the P self-impedance matrices $\bar{\mathbf{Z}}_{i,i}$ (related to $\mathbf{J}$ and $\mathbf{M}$). This avoids recalculating them during the computation of $\bar{\mathbf{Z}}_{R}$. The second one is for the storage of the PBFs of the P blocks, where $c = 2$ for POZ and $c = 1$ for POZ1. The last one corresponds to the storage of the reduce matrix $\bar{\mathbf{Z}}_{R}$. The memory requirement for the brute force MoM is $M_{\text{LU}} = (2P\bar{N}_{\text{Edge}})^2$.

At the top of Fig. 16, the ratio $M_{\text{LU}}/M_{\text{HCBFM}}$ (gain in memory requirement) is plotted versus N_{Edge}. As expected, this ratio increases as N_{Edge} grows, which means that HCBFM is efficient in terms of memory requirement in comparison to a brute force MoM.

In the middle of Fig. 16, the RACA mean compression ratio on the unconnected pair blocks is plotted versus N_{Edge}. The number of blocks is chosen such that the edge number per block remains constant and is of the order of 1400. As N_{Edge} increases, the number of blocks grows, and the number of unconnected block pairs also increases. In addition, the mean compression increases because the distance between the blocks grows. So, HCBFM hybridized with RACA is efficient for a large problem. It is important to underline that the precision of HCBFM is not deteriorated as N_{Edge} increases.

The time filling of the whole impedance matrix (LU solution; complexity of $\mathcal{O}(N_{\text{Edge}}^{2})$) is approximately 4–5 times faster than that obtained to calculate the CBFM sub-matrices. The explanation is that with CBFM, to compute the P^2 sub-matrices, the associated function (written

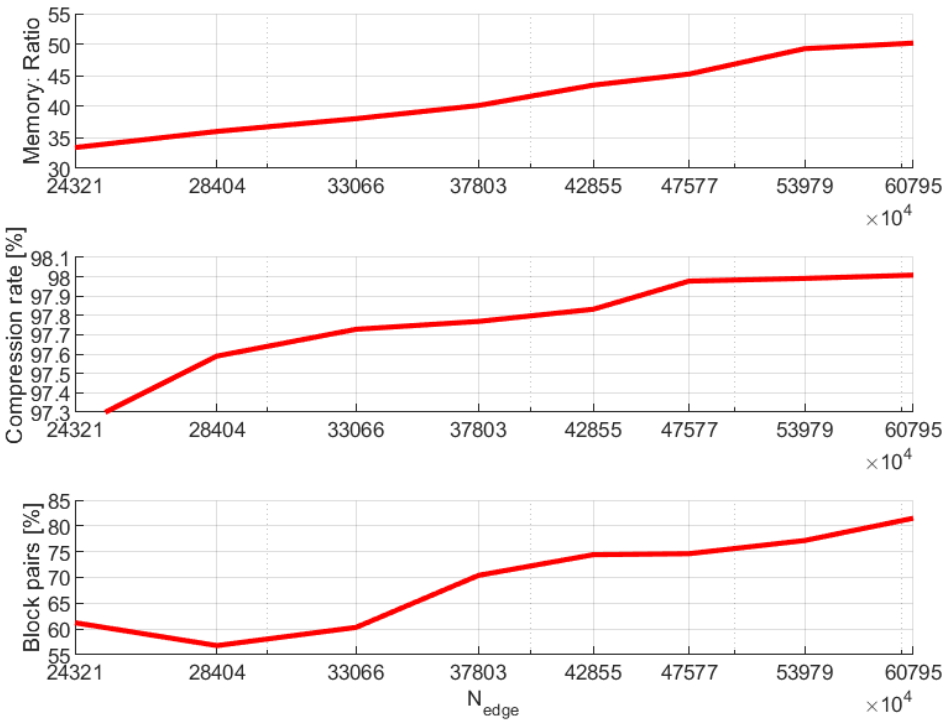

Figure 16. Top: Ratio $M_{\mathrm{LU}}/M_{\mathrm{HCBFM}}$ (gain in memory requirement) versus N_{Edge}. Middle: RACA mean compression ratio versus N_{Edge} on the unconnected pair blocks. Bottom: Percentage of the unconnected pair blocks versus N_{Edge}.

in C) is called P^2 times from MatLab, whereas only once for LU. When RACA is applied, the time filling of the unconnected coupling impedance matrices is strongly reduced.

4. CONCLUSION

In this paper, a new numerical scheme of CBFM is addressed to calculate the field scattered by a dielectric object. To expedite the calculation of the PBFs, related to the electric and magnetic currents, PO is applied. This approximation, named POZ, is obtained from the sparse EFIE impedance matrix. In addition, PO of Jakobus and Landstorfer (valid for a PEC surface) is extended to a dielectric surface, named POJ. The MECA, based on the tangent-Kirchhoff plane approximation, is also hybridized with CBFM. The numerical results show that HCBFM-POZ is valid for both a sphere and a cube whereas CBFM-MECA and HCBFM-POJ are only valid for a cube and are less accurate. We also show that the POZ PBFs of electric and magnetic currents are equal, which allows us accelerate the computation of the PBFs step, since the matrix size is to halve in comparison to the conventional CBFM. The use of the ACA compression accelerates the calculation of the characteristic matrix without altering the accuracy. POZ (or POZ1) needs a matrix inversion which makes this approximation more robust versus the surface curvature, unlike POJ and MECA, which do not require a matrix inversion. As shown in [34], since the POZ matrix is sparse, its inversion is strongly expedited by using a simple iterative algorithm.

REFERENCES

1. Harrington, R. F., *Field Computation by Moment Method*, Macmillan, New York, 1968.
2. Gibson, W. C., *The Method of Moments in Electromagnetics*, Chapman and Hall/CRC, London, 2008.

3. Quarteroni, A., R. Sacco, and F. Sameri, *Méthodes Numériques: Algortihmes, Analyse et Applications*, Springer-Verlag, New York, 2007.
4. Coifman, R., V. Rokhlin, and S. Wandzura, "The fast multipole method for the wave equation: A pedestrian prescription," *IEEE Antennas and Propagation Magazine*, Vol. 35, No. 3, 7–12, 1993.
5. Song, J. M., C. C. Lu, and W. C. Chew, "Multilevel fast multipole algorithm for electromagnetic scattering by large complex objects," *IEEE Transactions on Antennas and Propagation*, Vol. 45, No. 10, 1488–1493, 1997.
6. Jandhyala, V., E. Michielssen, B. Shanker, and W. C. Chew, "A combined steepest descent-fast multipole algorithm for the fast analysis of threedimensional scattering by rough surfaces," *IEEE Transactions on Geoscience and Remote Sensing*, Vol. 36, No. 5, 738–748, 1998.
7. Bleszynski, E., M. Bleszynski, and T. Jaroszewicz, "AIM: Adaptive integral method for solving large-scale electromagnetic scattering and radiation problems," *Radio Science*, Vol. 31, No. 5, 1225–1251, 1996.
8. Bagci, H., A. E. Yilmaz, J.-M. Jin, and E. Michielssen, *Modeling and Computations in Electromagnetics — Chapter 3: Time Domain Adaptive Integral Method for Surface Integral Equations*, H. Ammari, Ed., Springer, Berlin, 2000.
9. Ewe, W.-B., L.-W. Li, and M.-S. Leong, "Solving mixed dielectric/conducting scattering problem using adaptive integral method," *Progress In Electromagnetics Research*, Vol. 163, 143–163, 2004.
10. Colliander, A. and P. Yla-Oijala, "Electromagnetic scattering from rough surface using single integral equation and adaptive integral method," *IEEE Transactions on Antennas and Propagation*, Vol. 55, No. 12, 3639–3646, 2007.
11. Wang, X., S.-X. Gong, J. Ling, and X.-M. Wang, "Interpolation scheme based on adaptive integral method for solving electrically large radiation problem by surface/surface configuration," *Progress In Electromagnetics Research M*, Vol. 11, 203–211, 2010.
12. Zhou, L., L. Tsang, V. Jandhyala, Q. Li, and C. H. Chan, "Emissivity simulations in passive microwave remote sensing with 3-D numerical solutions of Maxwell equations," *IEEE Transactions on Geoscience and Remote Sensing*, Vol. 42, No. 8, 1739–48, 2004.
13. Huang, S. W., G. H. Zhang, M. Y. Xia, and C. H. Chan, "Numerical analysis of scattering by dielectric random rough surfaces using modified SMCG scheme and curvilinear RWG basis functions," *IEEE Transactions on Antennas and Propagation*, Vol. 57, No. 10, 3392–3397, 2009.
14. Liao, T.-H., L. Tsang, S. Huang, N. Niamsuwan, S. Jaruwatanadilok, S.-B. Kim, H. Ren, and K.-L. Chen, "Copolarized and cross-polarized backscattering from random rough soil surfaces from L-band to Ku-band using numerical solutions of Maxwell's equations with near-field precondition," *IEEE Transactions on Geoscience and Remote Sensing*, Vol. 54, No. 2, 651–662, 2016.
15. Qiao, T., L. Tsang, D. Vandemark, S. H. Yueh, T.-H. Liao, F. Nouguier, and B. Chapron, "Sea surface radar scattering at L-band based on numerical solution of Maxwell's equations in 3-D (NMM3D)," *IEEE Transactions on Geoscience and Remote Sensing*, Vol. 56, No. 6, 3137–47, 2018.
16. Bourlier, C., "Scattering from quasi-planar and moderate rough surfaces: Efficient method to fill the EFIE-Galerkin MoM impedance matrix and to solve the linear system," *IEEE Transactions on Antennas and Propagation*, Vol. 69, No. 9, 5761–5770, Jan. 2021.
17. Bourlier, C., N. Pinel, and G. Kubické, "Propagation-inside-layer-expansion method combined with physical optics for scattering by coated cylinders, a rough layer, and an object below a rough surface," *Journal of the Optical Society of America A*, Vol. 30, No. 9, 1727–1737, 2013.
18. Bourlier, C., S. Bellez, and G. Kubické, "Sub-domain decomposition iterative method combined with ACA: An efficient technique for the scattering from a large highly conducting rough sea surface," *IEEE Transactions on Antennas and Propagation*, Vol. 63, No. 2, 659–666, 2015.
19. Bellez, S., C. Bourlier, and G. Kubické, "An efficient PILE algorithm for solving the scattering from three-dimensional (3-D) nested homogeneous dielectric bodies," *Journal of the Optical Society of America A*, Vol. 32, No. 3, 392–401, 2015.

20. Bourlier, C., Y. Arencibia Noa, and G. Kubické, "Two domain decomposition methods, SDIM and CBFM, for the scattering from a two-dimensional perfectly-conducting rough surface: Comparison and parametric study," *Journal of the Optical Society of America A*, Vol. 37, No. 9, 1512–1525, 2020.
21. Suter, J. R. and E. Mosig, "A subdomain multilevel approach for the efficient MoM analysis of large planar antennas," *Microwave Optical Technology Letters*, Vol. 26, No. 4, 270–277, 2000.
22. Matekovits, L., V. A. Laza, and G. Vecchi, "Analysis of large complex structures with the synthetic-functions approach," *IEEE Transactions on Antennas and Propagation*, Vol. 5, No. 55, 2509–2521, 2007.
23. Prakash, V. S. and R. Mitra, "Characteristic basis function method: A new technique for efficient solution of method of moments matrix equations," *Microwave Optical Technology Letters*, Vol. 26, No. 2, 95–100, 2003.
24. Lucente, E., A. Monorchio, and R. Mittra, "An iteration-free MoM approach based on excitation independent characteristic basis functions for solving large multiscale electromagnetic scattering problems," *IEEE Transactions on Antennas and Propagation*, Vol. 56, No. 4, 999–1007, 2008.
25. Wang, Z. and P. Wang, "Application of characteristic basis function method based on characteristic mode theory to solve the monostatic RCS of objects," *International Applied Computational Electromagnetics Society Symposium*, Chengdu, China, Jul. 2021.
26. Bourlier, C., "Acceleration of the primary basic functions calculation from the CBFM-EFIE combined with the physical optics approximation," *IEEE Transactions on Antennas and Propagation*, Mar. 7, 2022.
27. Yagbasan, A., C. A. Tunc, V. B. Erturk, A. Altintas, and R. Mitra, "Characteristic basis function method for solving electromagnetic scattering problems over rough terrain profiles," *IEEE Transactions on Antennas and Propagation*, Vol. 58, No. 5, 1579–1589, 2010.
28. Laviada, J., M. R. Pino, and F. Las-Heras, "Generation of excitation-independent characteristic basis functions for three-dimensional homogeneous dielectric bodies," *IEEE Transactions on Antennas and Propagation*, Vol. 59, No. 9, 3318–3327, 2011.
29. Li, C. and R. Mittra, "Characteristic basis function method for fast analysis of 3-D scattering from objects buried under rough surfaces," *IEEE Transactions on Geoscience and Remote Sensing*, Vol. 57, No. 8, 5252–5265, 2019.
30. Huang, F. and Y. Sun, "Efficient solution of electromagnetic scattering from dielectric objects via characteristic basis function method based on large-size blocks with multilevel subdivision," *IEEE Access*, Vol. 7, 71 741–71 748, 2019.
31. Huang, F. and Y.-F. Sun, "Fast solution of electromagnetic scattering from dielectric objects via the modified SVD-CBFM," *IEEE International Conference on Computational Electromagnetics*, Shanghai, China, Mar. 2019.
32. Bourlier, C., "Rough layer scattering filled by elliptical cylinders from the method of moments combined with the characteristic basis function method and the Kirchoff approximation," *Journal of the Optical Society of America A*, Vol. 38, No. 10, 1581–1593, 2021.
33. Wan, J., H. Ye, and M. S. Tong, "An effective extraction method of common characteristic basis functions for 3D rough surfaces scattering computation," *Photonics & Electromagnetics Research Symposium*, Hangzhou, China, Nov. 2021.
34. Bourlier, C., "Acceleration of the primary basic functions calculation from the EFIE-Characteristic Basis Function Method (CBFM) combined with a new physical optics approximation," *Progress In Electromagnetics Research B*, Vol. 99, 179–195, 2023.
35. Jakobus, U. and M. Landstorfer, "Improved PO-MM hybrid formulation for scattering from three-dimensional perfectly conducting bodies of arbitrary shape," *IEEE Transactions on Antennas and Propagation*, Vol. 43, No. 2, 162–169, 1995.
36. Fung, A. K., *Microwave Scattering and Emission Models and Their Applications*, ser. Remote Sensing Library, Artech House, Boston, London, 1994.

37. Bellez, S., C. Bourlier, and G. Kubické, "3-D scattering from a PEC target buried beneath a dielectric rough surface: An efficient PILE-ACA algorithm for solving a hybrid KA-EFIE formulation," *IEEE Transactions on Antennas and Propagation*, Vol. 63, No. 11, 5003–5014, 2015.
38. Bebendorf, M., "Approximation of boundary element matrices," *Numer. Math.*, Vol. 86, No. 4, 565–589, 2000.
39. Bebendorf, M. and S. Rjasanow, "Adaptive low-rank approximation of collocation matrices," *Computing*, Vol. 701, No. 1, 1–24, 2003.
40. Zhao, K., M. N. Vouvakis, and J.-F. Lee, "The adaptive cross approximation algorithm for accelerated method of moments computations of EMC problems," *IEEE Transactions on Electromagnetic Compatibility*, Vol. 47, No. 4, 763–773, 2005.
41. Rao, S., D. Wilton, and A. Glisson, "Electromagnetic scattering by surfaces of arbitrary shape," *IEEE Transactions on Antennas and Propagation*, Vol. 30, No. 409-18, 1982.
42. Yaghjian, A. D., "Sampling criteria for resonant antennas and scatterers," *Journal of Applied Physics*, Vol. 79, No. 10, 7474–7472, 1996.
43. Fenni, I., H. Roussel, M. Darces, and R. Mittra, "Fast analysis of large 3-D dielectric scattering problems arising in remote sensing of forest areas using the CBFM," *IEEE Transactions on Antennas and Propagation*, Vol. 62, No. 8, 4282–4291, 2014.
44. Tsang, L., J. A. Kong, and K.-H. Ding, *Scattering of Electromagnetic Waves, Theories and Applications*, W. S. in Remote Sensing, Ed., John Wiley & Sons, Inc., 2000.
45. Park, C.-S., Y.-R. Jeong, I.-P. Hong, and J.-G. Yook, "Block size optimization of CBFM for scattering problems," *IEEE Transactions on Antennas and Propagation*, Vol. 66, No. 10, 5370–5377, 2018.